High-resolution structural imaging of volcanoes using improved muon tracking

R Bajou, M Rosas-Carbajal, A Tonazzo, J Marteau

submitted to *Geophys. J. Int.*

High-resolution structural imaging of volcanoes using improved muon tracking

R. Bajou[1], M. Rosas-Carbajal[1], A. Tonazzo[2], J. Marteau[3]

[1] *Université Paris Cité, Institut de Physique du Globe de Paris, Paris, France*

[2] *Université Paris Cité, CNRS, Astroparticule et Cosmologie, Paris, France*

[3] *Université de Lyon UCBL, Institut de Physique des deux infinis (CNRS UMR 5822), Villeurbanne, France*

SUMMARY

Muography is increasingly used to image the density distribution of volcanic edifices, complementing traditional geophysical tomographies. Here we present a new muon data processing algorithm, and apply it to a new generation of scintillator-based muon detectors, to image the relative density distribution in La Soufrière de Guadeloupe volcano (Lesser Antilles, France). Our processing method iteratively searches for the best fit of each muon trajectory, accounting for all the hits registered by the detector related to the particular muon event. We test the performance of our algorithm numerically, simulating the interaction of muons with our detector and accounting for its exact assemblage including the scintillator bars and lead shielding. We find that our new data processing mitigates the impact of spurious signals coming from secondary particles, and improves the amount of successfully reconstructed events. The resulting two-dimensional muon images at La Soufrière have higher angular resolution than previous ones and capture the heterogeneous structure of the dome. They show density anomalies located on the summit southern region, which includes a boiling acid lake and degassing fractures, where the rock is the most porous and fumarolic activity is ongoing. This work shows the importance of combining numerical simulations of muon propagation with precise raw data processing to obtain high-quality results. It is also a first step towards fully as-

sessing the noise contamination sources when performing muon tomography, and their correction, prior to geophysical interpretations.

Key words: Tomography – Volcano monitoring – Hydrothermal systems – Instrumental noise – Numerical modeling – Muography.

1 INTRODUCTION

Volcanoes are complex systems that vary significantly in terms of size, internal structure, and the dynamics of heat and mass transport from the magma chamber to the surface. These properties thus require dedicated studies for each particular volcano in order to understand their functioning and mitigate their potential hazards. Both active and dormant volcanoes carry potential edifice collapse hazards associated with their geometry and past activity, which usually leads to mechanically weak rocks and collapse-prone flanks (Heap & Violay, 2021).

Geophysical imaging is used to study the volcano's internal structure and is performed with different methods such as seismic, gravity, magnetotellurics, electrical resistivity tomography, and muography. Each of these methods is sensitive to the spatial distribution of a particular physical property, but they all provide complementary information useful to 1) determine regions of different rock types, in particular places where the rock has been altered or is naturally mechanically weak; 2) understand the magmatic and meteoric fluid pathways, the potential chemical reactions, and the heat transport dynamics inside the volcano; 3) relate processes detected in the surface to the main geological structures; and 4) calibrate numerical models meant to explain the volcano functioning. When information about possible unstable and/or altered rock is available, failure surfaces can be suggested to test numerically the velocity and final emplacement of debris avalanches (Peruzzetto et al., 2019).

Muography is a relatively novel method used to image the density distribution inside volcanic edifices (Tanaka, 2018; Marteau et al., 2016; D'Alessandro et al., 2018). Its imaging principle relies on particle absorption and deviation in a dense medium. The natural muon flux resulting from the interaction of cosmic rays with the atmosphere arrives at the Earth's surface and decreases as the muons traverse a dense structure. The decrease in the muon flux is a function of the mean density of the crossed medium along the muons' trajectory. A muon detector measures the flux of muons exiting the volcano along different directions or lines of sight. Thus, two-dimensional (2-D) muon-based images (hereafter called *muographies*) of the mean density in the different lines of sight can be obtained.

Originally used to characterize the natural rock shielding overlying underground particle physics laboratories in the 1950s, muon absorption imaging was then transported towards archaeological

studies and turned into an in situ experiment, by Alvarez et al. (1970), during an imaging campaign performed on the Chephren pyramid of the Giza ancient Egyptian complex. This pioneer field measurement and feasibility demonstration lead the path towards the applications that are used these days in volcanic structure imaging, with the first measurements led by Japanese teams in the 1990s (Nagamine et al., 1995). Repeating muon measurements at several positions around a volcano, the final goal is to combine the 2-D mean density images to compute a three-dimensional (3-D) density model, as reported by (Rosas-Carbajal et al., 2017; Nishiyama et al., 2017; Barnoud et al., 2021). The analogy with medical X-ray CT-scan is thus often made in the literature. The reader is invited to refer to Bonechi et al. (2020) for an exhaustive review of the muon imaging physics and detection technology, and to Lechmann et al. (2021) for a specific state of muography applications in geosciences.

La Soufrière de Guadeloupe is a volcano located in the Lesser Antilles belonging to France's overseas territory and classed as one of the most dangerous in terms of its active hydrothermal system (Siebert et al., 2011). Not only responsible for sudden violent eruptions without magmatic juvenile material involved (the last major crisis occurred in 1976-1977), hydrothermal activity (Komorowski, 2005; Tamburello et al., 2019; Moretti et al., 2020; Moune et al., 2022) and the resulting rock alteration process plays a major role in the destabilization of the structure, which worsens the risk of slope failure and partial flank collapse (Heap et al., 2021; Ball et al., 2015). In addition to established geophysical methods such as seismic tomography, gravimetry surveys, muon absorption imaging, referred to in the literature as muography, or simply muography, has now become part of the imaging tools available to map out density profiles of geological bodies such as volcanic dome, and identify density variations relative to acid hydrothermal fluid circulation.

Since the early 2010s, scintillator-based particle trackers, referred to in the following as muon telescopes, were developed at IP2I, Lyon, and deployed on the field at different locations around La Soufrière de Guadeloupe flanks. The goal was to perform dynamic muon absorption imaging of the andesitic lava dome. These campaigns have set the ground for inserting muon imaging into the scope of conventional monitoring at La Soufrière, as a non-invasive tool. Conjointly with other geophysical and geochemical methods, they have indeed enlightened the hydrothermal system dynamics inside the volcanic edifice and its effects on the rock density (Lesparre et al., 2012a; Jourde et al., 2016).

Three-dimensional density models have been inferred, notably by joint inversion of muon and gravimetry datasets by Rosas-Carbajal et al. (2017), putting forward several low-density anomalies on the southern volcano flank, presumably in the areas where the rock is highly porous and mechanically weaken by the acid fluid circulation. Furthermore, as scintillator detectors offer time information on the muon arrival, continuous monitoring of sudden destabilization in the hydrothermal activity has been explored on time scales of hours and days (Gonidec et al., 2019) through the combination of muon data with seismic signal backed up with vent temperature measurements, highlighting strong

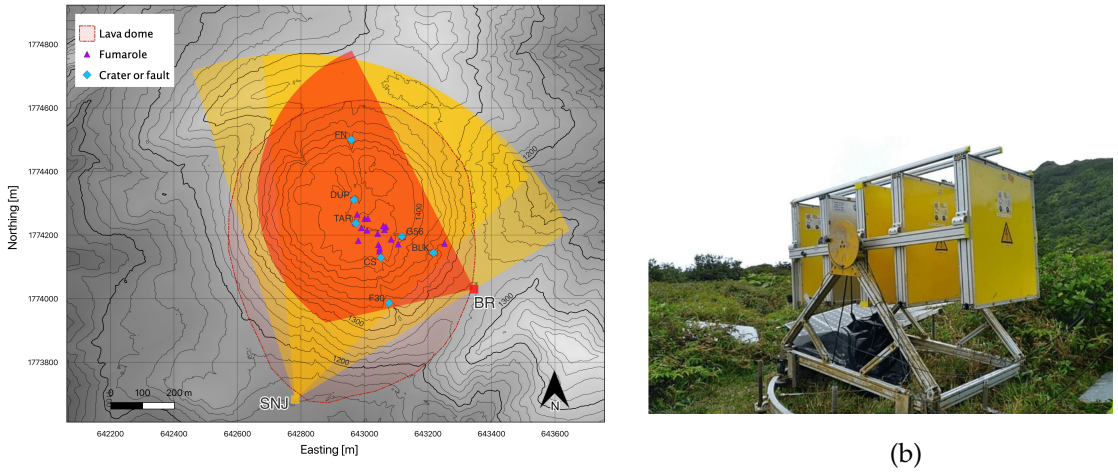

(a)

(b)

Figure 1. (a) Map of La Soufrière lava dome featuring locations of the two telescopes SNJ and BR and their respective angular acceptance. The SNJ telescope has a 4-panel configuration and covers two regions at the same time: a broader region in light yellow shade with its 3-panel sub-configuration, and a tightened region using the 4-panel configuration. The main structural features, notably the Tarissan (TAR) and South (CS) craters, and active fumarolic vents on the dome summit are encompassed by both telescope angular apertures. (b) Photo of the SNJ telescope during its assembly, located at the South-West of the dome, composed of 4 detection matrices and an additional lead shielding panel at the center.

correlations between the three signals over a 3-day period, interpreted as the first multi-sensor hydrothermal activity identification.

To this day, muon telescope data at La Soufrière were reconstructed using a fast and simple tracking principle: a straight-trajectory check of the most-energetic hits on the 3 scintillator panels. But muons are not the only particles generating a signal in scintillator panels, and often many hits per panel are observed in what is registered as a single "event". Muons are indeed expected to form a straight track in the detector, and they are minimum ionizing particles, which implies that their associated energy deposit in the scintillator medium - of the order of 2 MeV/(g.cm^{-2}) - is not the highest possible on each panel. Therefore this kind of selection is already biased by the presence of other types of particles generated in atmospheric showers. Furthermore, depending on the relative angle between the muon trajectory and the detector orientation, a single muon can traverse more than one scintillator "pixel" per panel. A solid fit procedure of the hits is thus necessary to retrieve the correct muon trajectory and cope with contamination from other atmospheric particles and spurious hits formed by instrumental noise (e.g. optical or electrical cross-talks, dark counts arising in time coincidence).

In this paper, we present a new method to process the raw muography data, which improves the reconstruction of detected muons. Our tracking algorithm is based on a random sampling consensus procedure *RANSAC* (Fischler & Bolles, 1981), which provides the best fit to the particle trajectory con-

sidering all the panel hits involved in a single event. To evaluate the performance of our algorithm, we use the GEANT4 Monte-Carlo simulation framework for particle propagation (Agostinelli et al., 2003), and assess the reconstruction efficiency. Finally, we apply our algorithm to novel data acquired at La Soufrière de Guadeloupe by two muon detectors. We provide the relative density muographies and interpret them in terms of the main geological features observed at the volcano.

2 METHODOLOGY

2.1 Muon detection

Scintillator-based particle detectors are well-established tools for muography (Tanaka et al., 2003; Marteau et al., 2012; Saracino et al., 2016; Lo Presti et al., 2020; Peña-Rodríguez et al., 2020). With their robust, modular, and relatively simplified design compared to high-energy physics detectors, they are appropriate to deal with the main challenge of rough field operations (Lesparre et al., 2012a).

Since 2017 two muon telescopes, respectively equipped with four and three scintillator panels, are installed at two different locations around the La Soufrière lava dome: at the South-West, and East of the volcano whose positions are shown in Fig. 1.

The novel 4-panel configuration (4p), in addition to decreasing the low-energy particles background, allows increasing spatial resolution on the 2D density muography of the central part of the dome scanned region and offers two more 3-panel sub-configurations (3p1 and 3p2), which lead finally to three different muon images.

As represented in Fig. 1, the 4-panel telescope named *SNJ* allows scanning at the same time a broad angular region using signal recorded in three panels with respective azimuth and zenith angles $(\varphi_{3p}, \theta_{3p}) \in ([-17; 58]^\circ, [43; 107]^\circ)$, as well as a narrower angular region centered on the dome bulk and its two main craters, using all 4 panels: $(\varphi_{4p}, \theta_{4p}) \in ([-5; 46]^\circ, [52; 98]^\circ)$. The two geometrical configurations have thus different angular acceptances. SNJ includes 4 detection matrices (front, middle1, middle2, and rear) interspaced by 60 cm; each matrix is an array of 16x16 bars, which is 80 cm long, 1 cm thick, and 5 cm wide.

The 3-panel telescope, named *BR*, is located on the Eastern flank. It has 3 matrices (front, middle and rear) also interspaced by 60 cm: the front and rear matrices are composed of 32x32 bars, 80 cm long, 1 cm thick, and 2.5 cm wide, while its middle matrix ensures signal coincidence without affecting the total number of lines-of-sight and thus presents a lower pixel resolution with a 16x16 bar configuration, similar to SNJ matrices. All the matrices have the same detection area of 80x80 cm^2.

Each scintillator bar has its own wavelength-shifter (WLS) fiber embedded within the scintillator medium to conduct the light towards a multi-anode photomultiplier (MAPMT), with 64 channels. One MAPMT per detection matrix takes care of the light signal conversion to electrons and ampli-

fication before processing by the readout electronics described in Marteau et al. (2012). A simple straight-line interpolation of the signals in the first and last plane would provide an angular resolution of 12 mrad (3p) or 8 mrad (4p) for SNJ and of 6 mrad for BR.

In addition to the detection matrices, a 100 mm thick lead shielding panel has been installed on both telescopes behind the middle matrix, compatible with mechanical constraints on the structure. This passive shielding allows for stopping low-energy particles. We estimated its cutoff energy to be around 170 MeV, using the numerical simulations explained later on in this work. The shielding also triggers electromagnetic showers, composed of secondary electrons and photons, characterized by a high hit multiplicity on the rear panel. Detailed descriptions of the muon telescope assembly used in this study can be found in Lesparre et al. (2012a) and Jourde et al. (2014); and description of the light and electronic readout as well as the timing system in Marteau (2009), Marteau et al. (2012), and Jourde et al. (2014).

2.2 Rock density estimation

In muon absorption tomography, the observable is the number of reconstructed particle tracks N detected by the muon telescope during a period of time ΔT, for each line-of-sight $\mathbf{r}_{i,j}$ where (i,j) represents a given front-rear pixels combination. Assuming a point-like telescope in comparison to the size of the scanned object, each (i,j) corresponds to a unique (θ,φ) angular direction. The detector is characterized by a direction-dependent experimental acceptance $\mathcal{T}_{\text{exp}}$, which accounts for the telescope geometry, as well as instrumental and reconstruction effects. To estimate $\mathcal{T}_{\text{exp}}$, the telescope is placed in open-sky mode during a calibration run, in a vertical position, that is, the central axis at zenith $\theta = 0°$, and the following quantity is derived:

$$\mathcal{T}_{\text{exp}}(\mathbf{r}_{i,j}) = \frac{N^{\text{sky}}(\mathbf{r}_{i,j})}{\Delta T^{\text{calib}} \times I^{\text{sky}}(\mathbf{r}_{i,j})} \quad [\text{cm}^2.\text{sr}] \tag{1}$$

where $N^{\text{sky}}(\mathbf{r}_{i,j})$ is the number of open-sky muons detected in $\mathbf{r}_{i,j}$, ΔT^{calib} is the calibration run duration (around two days). The open-sky muon integral flux $I^{\text{sky}}(\mathbf{r}_{i,j})$ is estimated with CORSIKA (Heck et al., 1998), a Monte-Carlo simulation tool that allows accurate cosmic muons flux estimation. CORSIKA propagates extensive atmospheric showers, from their generation by primary cosmic-ray, e.g. an extra-galactic proton, interactions on upper atmosphere nuclei to their ground-level detection. Furthermore, this detailed MC framework allows us to consider geomagnetic effects alongside atmospheric parameters (e.g. density variations through a layered atmosphere model) that affect the muon flux, as studied in Cohu et al. (2022).

Once the acceptance has been calculated, the telescope is oriented towards the volcano and the transmitted muon flux noted I^{data} can be estimated for each line-of-sight $\mathbf{r}_{i,j}$ with the following expression:

$$I^{\text{data}}(\mathbf{r}_{i,j}) = \frac{N(\mathbf{r}_{i,j})}{\Delta T \times \mathcal{T}_{\text{exp}}(\mathbf{r}_{i,j})} \quad [\text{cm}^{-2}.\text{s}^{-1}.\text{sr}^{-1}] \tag{2}$$

where $N(\mathbf{r}_{i,j})$ is the number of transmitted muon candidates along $\mathbf{r}_{i,j}$, ΔT is the tomography run duration, and $\mathcal{T}_{\text{exp}}(\mathbf{r}_{i,j})$ is the experimental acceptance in $\mathbf{r}_{i,j}$, defined in Eq. 1.

In order to infer density values from $I^{\text{data}}(\mathbf{r}_{i,j})$, a comparison with reference muon flux after attenuation in rock is necessary. The reference transmitted flux noted $I^{\text{calc}}(\varrho, \theta)$ depends on the zenith angle θ and on the crossed amount of matter, quantified in muography with a parameter called *opacity* ϱ, defined as the integral of density ρ along rock thickness L:

$$\varrho(L) = \int_L \rho(\xi)\, d\xi \quad [\text{g.cm}^{-2}] \tag{3}$$

As for the experimental acceptance computation (cf. Eq. 1), $I^{\text{calc}}(\varrho, \theta)$ is estimated from Monte-Carlo simulation e.g. CORSIKA, computationally intensive but more accurate at the observation site for the reasons mentioned before than semi-analytical models (e.g. (Gaisser et al., 1990; Guan et al., 2015)) based on the muon production from mesons in the high atmosphere. A computation for each opacity of the muon minimal crossing energy E_{min} is required to obtain the transmitted muon flux for a known density distribution. For this purpose, the work of the Particle Data Group (Workman & Others, 2022) is widely used. It provides an exhaustive review of the different interaction processes at stake, and their associated energy deposit contributions, during muon propagation in a dense medium. Finally, the muon energy spectrum $\Phi(E, \theta)$ can be integrated over $[E_{\text{min}}(\varrho); +\infty[$:

$$I^{\text{calc}}(\theta, \varrho) = \int_{E_{\text{min}}(\varrho)}^{+\infty} \Phi(E, \theta)\, \mathrm{d}E \quad [\text{cm}^{-2}.\text{s}^{-1}.\text{sr}^{-1}] \tag{4}$$

Once the opacity is estimated from data-model flux comparison, a mean density value can be obtained for each line-of-sight $\mathbf{r}_{i,j}$: $\overline{\rho}_{i,j} = \varrho_{i,j}/L_{i,j}$.

2.3 Data processing

Along with the energy deposits (so-called *hits*) generated by muons crossing the detector and used to reconstruct their trajectories, other sources induce signals in the scintillator bars: other atmospheric particles from electromagnetic and hadronic components of atmospheric showers, secondary background particles (electrons and photons) produced inside the detection volume, or instrumental noise caused notably by random emission of electrons from the MAPMT photo-cathode and cross-talks. To mitigate their impact on the track reconstruction process, we present a new track reconstruction algorithm that considers the presence of these "outlier" hits. The tracking algorithm was written in Python, with the use of the *ransac* module available in the *scikit-image* library (van der Walt et al.,

2014). The fit procedure is also useful in the context of the 4-panel telescope configuration, to account for detection inefficiencies: for muons forming hits in only 3 panels, but contained in the 4-panel angular region, the trajectory model allows to extrapolate the muon position in the untouched panel.
Our event-by-event track fitting procedure lies on an hypothesize-and-test iterative process, called random sample consensus RANSAC (Fischler & Bolles, 1981). The different steps of the reconstruction workflow are represented in Fig. 2. First, we filter out events presenting a number of hits per panel larger than 10, which are likely to be due to an electromagnetic shower, or impacting less than 3 detection panels. The process starts by randomly sampling within the hit coordinates, a subset of points of a given size, and fitting a hypothesized line model to this subset. It then evaluates which hits of the whole dataset are consistent with this hypothesized model, computes a fit error, and counts the number of hits whose orthogonal distance to the model is below a given distance threshold t (set to one scintillator width). Those hits form the consensus set. The size of the initial sample s and the maximal number of iterations N_{max} were set to maximize the number of muon hits tagged as inliers, using the simulation of an open-sky muon run with the framework described in Section 2.4. After N_{max} iterations, the algorithm outputs the model that minimizes the fit error and maximizes the size of the consensus set. The hits belonging to the consensus are tagged as 'inliers' and the rest of the hits as 'outliers'. This method manages to increase the number of reconstructed muons and to improve the angular precision on the incident particle direction, compared to the former reconstruction algorithm used, relying on the check of the alignment of the most-energetic hits, i.e a check of the "straightness" of the track. A comparison of the two methods has been studied in Bajou et al. (2022).

2.4 Numerical simulations

Developing simulations for particle detectors in muography, as in all particle physics experiments, represents a crucial step to a better understanding of the detector and its response to particles of interest. More precisely, it allows estimating detection efficiency, a key parameter for quantifying the performance of our tracking algorithm. The most widespread tool for this purpose, the GEANT4 toolkit (Agostinelli et al., 2003) offers a framework with an exhaustive set of physics models to simulate particle interactions and tracking through a detailed numerical replica of the detector. The simulated signals can then be formatted as real data to test the reconstruction algorithm. Examples of simulated 10 GeV/c electron and muon events are shown in Fig. 3. The electron event in Fig. 3a is filtered out thanks to the 7-cm thick shielding panel between the middle 1 and middle 2 panels. The muon track in Fig. 3b is reconstructed with RANSAC. Along with the physical muon hits, Fig. 3b features outlier hits that were randomly added to the muon event signal. These "synthetic" hits were not assigned any intensity value (i.e. deposited energy) as this parameter is not considered in the current tracking workflow. This reconstructed event display illustrates the ability of the RANSAC procedure to

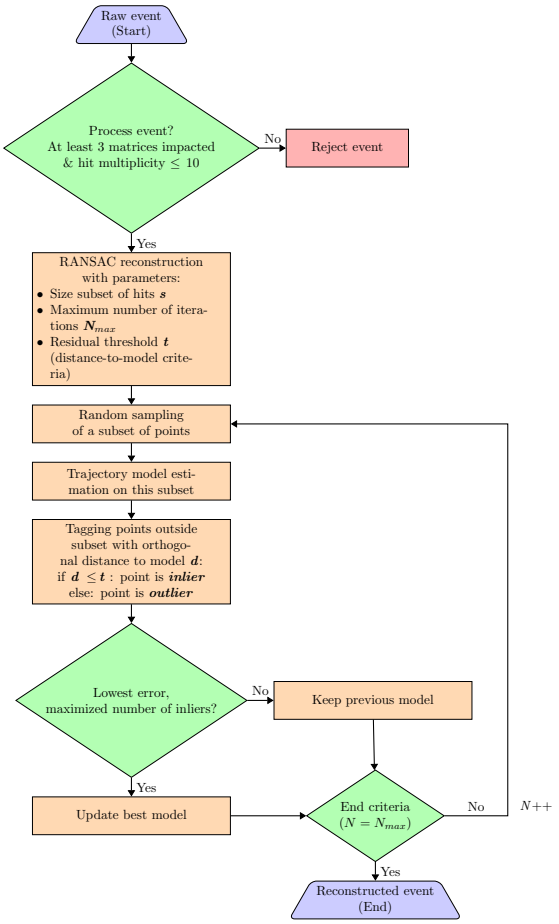

Figure 2. Data processing algorithm flowchart based on the RANSAC method.

fit the correct muon trajectory from a data set polluted by hits generated by instrumental effects like a deficient optical coupling between optical fibers, dark current arising from the photo-cathode and dynodes in MAPM, electronic cross-talk between MAPM channels.

3 RESULTS

3.1 Reconstruction performances

In the following section, we characterize the performance of our muon tracking algorithm for a 4-panel telescope. For this purpose, we use the GEANT4 simulation setup described in Section 2.4. We simulate an open-sky acquisition and write the muon hits recorded in the scintillator panels following the real telescope raw data format. Then, we use our algorithm to reconstruct the particle tracks following the reconstruction outline depicted in Fig. 2. Because we know the exact particle trajectories from the GEANT4 simulations, we can assess the tracking algorithm's performance. The results presented hereafter were obtained on a pure-muon sample of 10^7 events simulated in GEANT4 with energies $E_\mu \in [1, 10^6]$ MeV. Within this sample, we estimated that 7% of the generated muon tracks contained in the 4-panel acceptance cone are being absorbed in the detector shielding, before im-

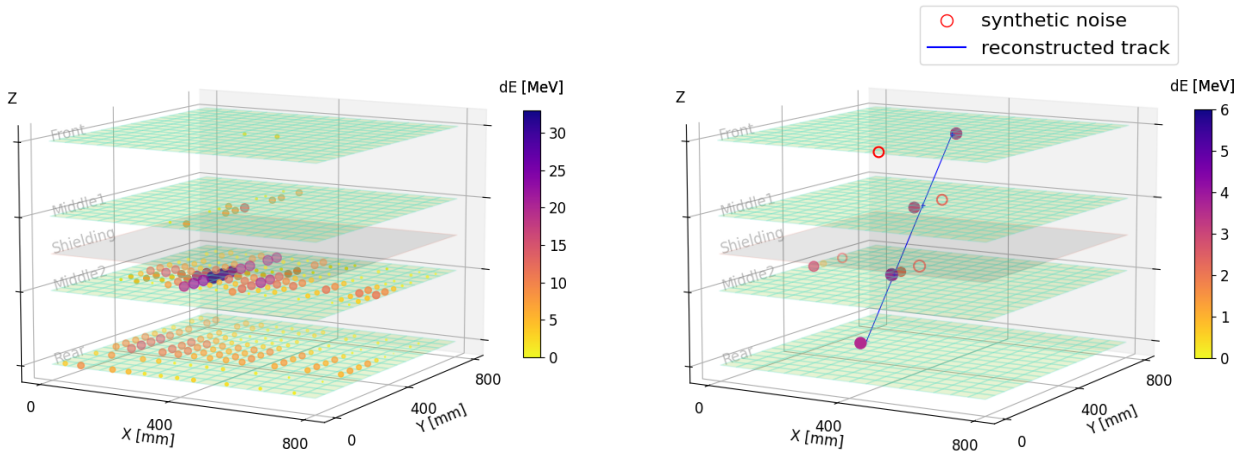

(a) Filtered 10 GeV.c^{-1} electron (MC)

(b) Reconstructed 10 GeV.c^{-1} muon (MC)

Figure 3. Three-dimensional representations of the hits formed in the telescope scintillator panels by: (a) an electromagnetic shower, triggered by the interaction of the primary electron with the shielding panel located between the Middle1 and Middle2 panels; (b) a simulated muon reconstructed with the RANSAC tracking algorithm, artificially polluted with synthetic outlier hits. The color scale represents the sum of energy deposits in X and Y bars, noted dE. The size of the XY hit is also proportional to dE. This information is however not used in the tracking algorithm.

pacting the rear detection matrix. The RANSAC tracking algorithm allows extrapolating the muon intersection position on this rear matrix.

3.1.1 Influence of secondary particles

Secondary electrons and photons produced by high-energy muons inside the detection volume, notably after crossing the shielding panel, impact the quality of the reconstruction of the incident muon trajectory. The RANSAC tracking allows for mitigating the impact of those spurious hits. In Fig. 4 we show the comparison between the real particles obtained in GEANT4 and the hit tagging performed by the algorithm. For initial sample size $s = 2$ and $N_{\max} \geq 20$ the true muon hit inlier fraction reaches a plateau at $98.4 \pm 0.2\%$. Besides, the muon tracking result also shows relatively low contamination from electrons and photons: these secondary hits represent $14.3 \pm 0.7\%$ of the total hits, and nearly half of this fraction ($6.7 \pm 0.6\%$) have been tagged as outliers.

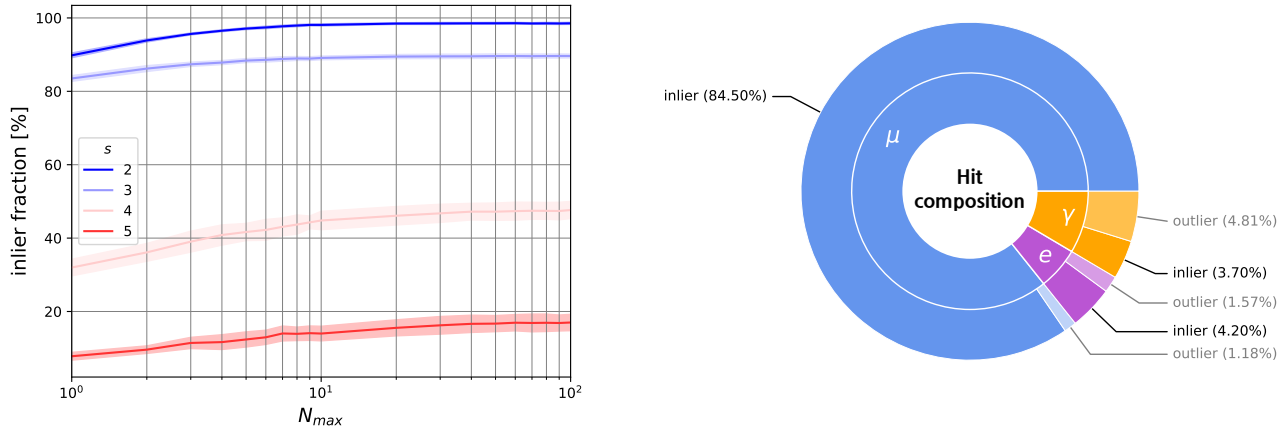

(a) (b)

Figure 4. Results of RANSAC tracking on simulated muon sample: (a) fraction of muon hits tagged as inliers as a function of the maximal number of iterations N_{max}, for different sizes of initial sample s; (b) composition of the XY hits formed by muons μ, and secondary particles: electrons e and photons γ, resulting from the interaction of muons with the detector. The inner circle represents the recorded hit composition from GEANT4 particle identification. The outer circle represents the proportion of hits tagged by the tracking algorithm as *inliers* and *outliers*. The RANSAC parameters have been set to $t = 50$ mm, $N_{\text{max}} = 20$, and $s = 2$.

3.1.2 *Reconstruction efficiency*

To assess the reconstruction efficiency $\varepsilon_{\text{reco}}$ of our tracking algorithm, we computed for each pixel corresponding to a given line of sight $\mathbf{r}_{i,j}$, the ratio between the number of RANSAC-reconstructed primary muons and the number of generated primary muons in GEANT4 :

$$\varepsilon_{\text{reco}}^{\text{MC}}(\mathbf{r}_{i,j}) = \frac{N_{\text{reco}}(\mathbf{r}_{i,j})}{N_0(\mathbf{r}_{i,j})} \tag{5}$$

where N_{reco} is the number of reconstructed muons, and N_0 is the number of primary muons.

The reconstruction efficiency obtained with the GEANT4 simulation $\varepsilon_{reco}^{\text{MC}}$ (cf. Eq. 5) can be compared with the reconstruction efficiency estimated with open-sky calibration data, which we defined as the following:

$$\varepsilon_{reco}^{\text{DATA}}(\mathbf{r}_{i,j}) = \frac{\mathcal{T}_{\text{exp}}(\mathbf{r}_{i,j})}{\mathcal{T}_{\text{geo}}(\mathbf{r}_{i,j})} \tag{6}$$

that is the ratio between the experimental detector acceptance $\mathcal{T}_{\text{exp}}$ (cf. Eq. 1), and the geometrical acceptance $\mathcal{T}_{\text{geo}}$, whose analytical expression is only a function of the telescope geometrical parameters: distance between the front and rear detection matrices, number, length, and width of the scintillator bars in each matrix (Sullivan, 1971; Thomas & Willis, 1972). Examples of efficiency maps obtained with the simulation and with real open-sky calibration data are shown in Fig. 5.

The reconstruction efficiency depends on the detection efficiency of the scintillator bars $\varepsilon_{\text{scint}}$, that

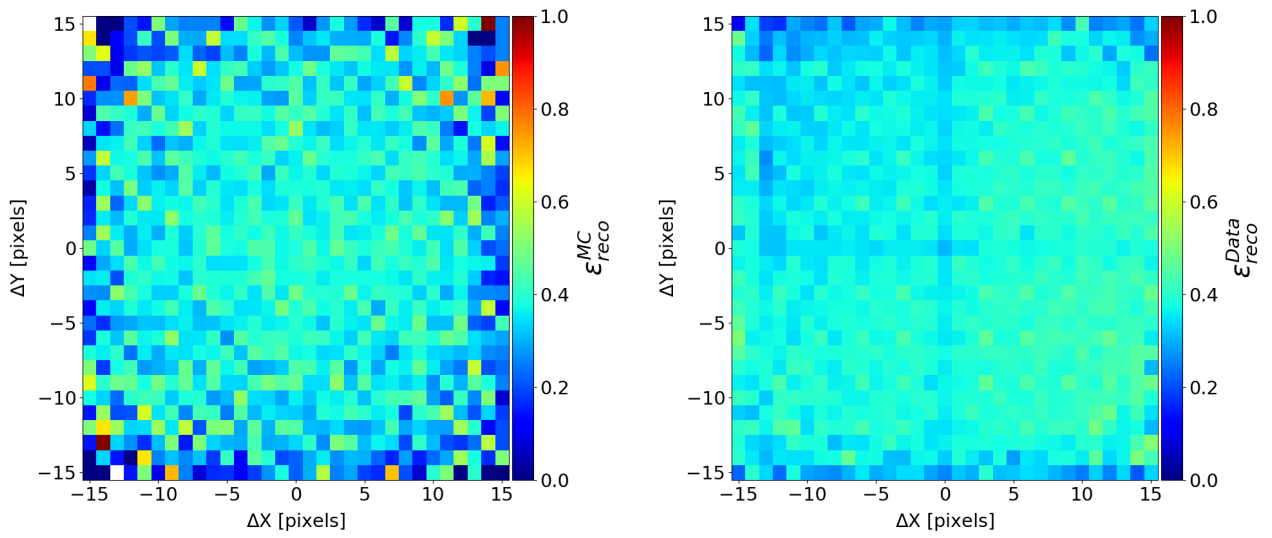

(a) (b)

Figure 5. Reconstruction efficiency maps for a 4-panel detector estimated from (a) Monte-Carlo simulated muons with GEANT4 reconstructed with RANSAC considering a scintillator efficiency of $\varepsilon_{\text{scint}} = 0.87$, and (b) a real 4-panel detector data.

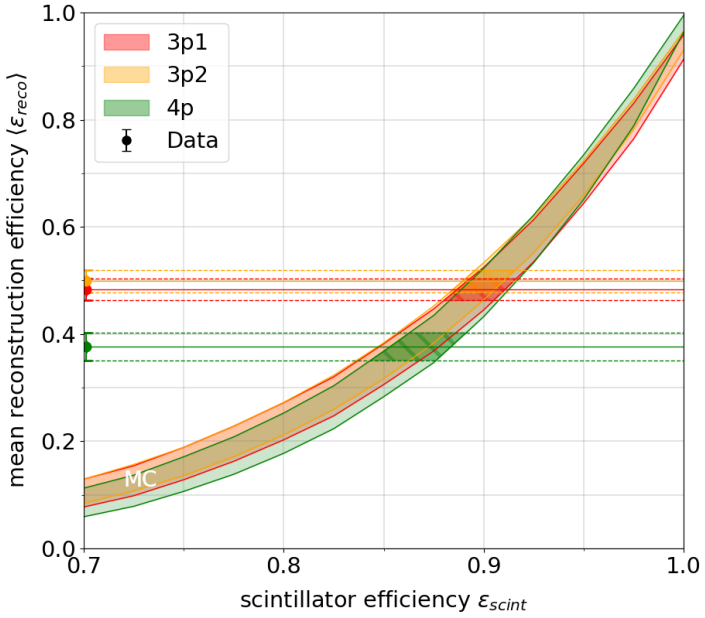

Figure 6. Mean reconstruction efficiency $\langle\varepsilon_{\text{reco}}\rangle$ as a function of scintillator efficiency parameter $\varepsilon_{\text{scint}}$, obtained from the muon MC simulation in GEANT4 (colored bands). The efficiency is derived for each of the three 4-panel telescope configurations: 3p1, 3p2, and 4p. The figure features calibration open-sky data points for each of the configurations. The hatch regions correspond to the intersection of the MC efficiency bands with the data uncertainty bands of the same configuration.

is, the probability for a given hit in a scintillator bar to give a signal above the threshold. We assume $\varepsilon_{\text{scint}}$ to be the same for all X and Y bars over each panel, although small differences from one bar to another occur in reality due to instrumental effects such as a deficient optical coupling between fibers and the light readout system (cf. Sec. 2.1). In Fig. 6, we show how the mean efficiency $\langle \varepsilon_{\text{reco}}^{\text{MC}} \rangle$ as a function of the $\varepsilon_{\text{scint}}$ parameter. From this relation, and using the mean data reconstruction efficiency $\langle \varepsilon_{\text{reco}}^{\text{DATA}} \rangle$, it is straightforward to interpolate the real telescope scintillator efficiency. We consider here the acceptance measurements performed on a 4-panel telescope (see Fig. 1b). As a result, we obtained the following scintillator efficiencies for the 3-panel and 4-panel events respectively: $\varepsilon_{\text{scint}}^{3p1} = 0.899 \pm 0.012$, $\varepsilon_{\text{scint}}^{3p2} = 0.900 \pm 0.010$ and $\varepsilon_{\text{scint}}^{4p} = 0.868 \pm 0.015$. These are consistent with the instrumental efficiency of the order of 0.9 usually considered for the technology of plastic scintillator bars with optical fiber readout employed in our detectors (Lesparre et al., 2012a).

3.2 Tomography data analysis

We present in this section the results obtained by applying our tracking algorithm (cf. Sec. 2.3) to real muon tomography data acquired by two muon telescopes (cf. Sec. 2.1): SNJ and BR, respectively located at South-West and East of the La Soufrière lava dome (cf. Fig. 1a).

The SNJ tomography dataset contains 1.9×10^7 reconstructed events acquired over a total run duration of 145 days in steady operation conditions (excluding dead time superior to one hour), between February and August 2019. The BR acquisition period ran from February 2018 to August 2019 over 547 steady days and contains 1.2×10^7 events. Both tomography runs were preceded by a 2-day long open-sky calibration run. Following the methodology explained in Sec. 2, the detector experimental acceptance is first estimated from calibration runs, then the incoming transmitted muon flux for each detector can be calculated, including the 3- and 4-panel configurations of detector SNJ.

To quantify the agreement between the data-estimated and modeled transmitted fluxes for different density values we use a Pearson χ^2-test :

$$\chi^2(\theta, \overline{\rho}) = \sum_{i,j}^{N_{\text{los}}} \left(\frac{I^{\text{data}}(\mathbf{r}_{ij}) - I^{\text{calc}}(\theta, \overline{\rho} L_{ij})}{\sigma_I(\mathbf{r}_{ij})} \right)^2 \tag{7}$$

where N_{los} is the total number of lines of sight at a given θ, and σ_I is the statistical uncertainty on the estimation of I^{data}.

We have chosen to present the following analysis results for both telescopes in terms of relative mean density variations rather than absolute density whose estimation suffers from irreducible background pollution (see Sec. 4). We then consider the quantity $\Delta\overline{\rho}$ defined with respect to the average value $\rho_0 = \langle \overline{\rho} \rangle$ from each telescope muography: $\Delta\overline{\rho} = (\overline{\rho} - \rho_0)/\rho_0$. Figure 7 shows on a given azimuth range $[\varphi_c - 2.5, \varphi_c + 2.5]^\circ$ (where φ_c is the central telescope azimuth) how the χ^2 varies as a function of $\Delta\overline{\rho}$ and zenith angle θ for each muon telescope. The chosen azimuth range targets for both tele-

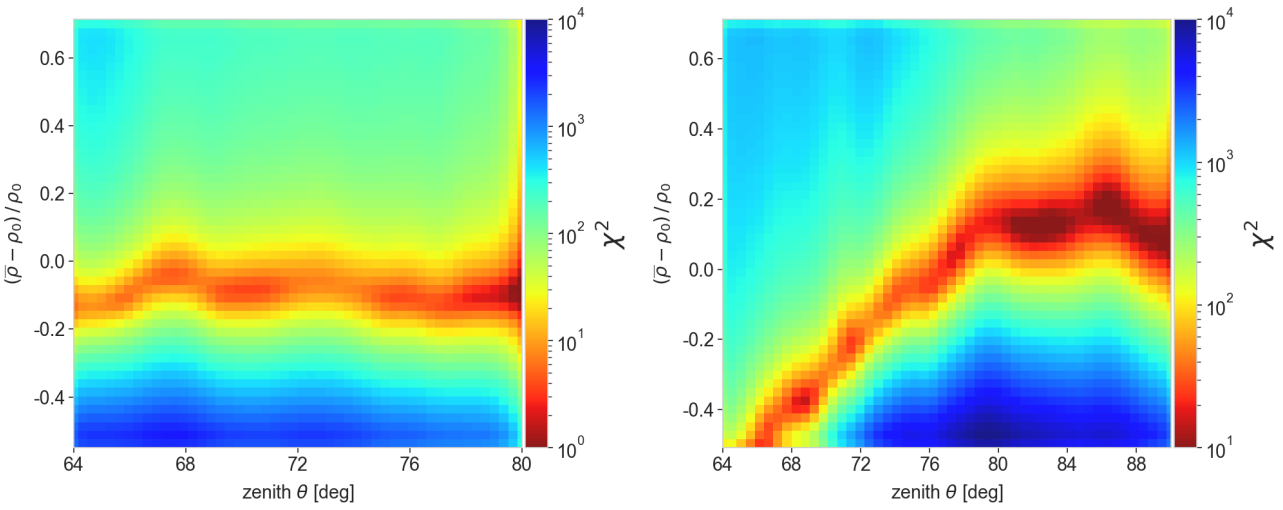

(a) (b)

Figure 7. χ^2 distribution (cf. Eq. 7) between estimated and calculated fluxes as a function of (θ, $\Delta\bar{\rho}$) on a $5°$-wide azimuth range around telescope central azimuth, for (a) SNJ and (b) BR datasets.

scopes the lava dome region beneath the Tarissan crater (TAR on Fig.1a, roughly 100 m deep from the dome surface which represents a vertical angular range of $\Delta\theta \simeq 10°$). The observed variations reflect the sensitivity to spatial variations of density. On the chosen azimuth range, we observe rather constant relative density in Fig. 7a located between -14.3% and -4.6% on the whole θ range. On the contrary, BR in Fig. 7b presents a stiff increase in $\Delta\bar{\rho}$ from -50.0% for smaller θ up to $+18.2\%$ at $\theta = 86.5°$, which directly echoes the increase in density from the shallow region close to the surface to the deeper part of the dome.

We now focus on the mean density spatial variations. Since the SNJ detector consists of 4 panels, we show in Fig. 8 the results for the 3- and 4-panel estimates. The measurements obtained by this telescope give evidence of significant density variations. The lowest values around -60% with respect to the mean ρ_0, are found for line of sights along the west flank for azimuth $\varphi \leq 10°$ close to the surface, and for the highest zenith values, corresponding to horizontal lines of sight in the east side (-30%). Besides these extreme values found on the borders, we see inside the dome a tendency from west to east from lower to higher average densities. The largest density values are indeed observed on the east side of the dome reaching up to $+70\%$ for azimuth $\varphi \geq 40°$.

The 4-panel image shown in Fig. 8 b) is a more detailed, "zoomed" version of Fig. 8 a). We see that both muographies are consistent, although the muon events used for the 4-panel acquisition naturally comprise fewer muon events than the 3-panel radiography. Since this radiography provides a better spatial resolution in the zone of interest, we present this case in Figs. 8 c) and d), a satellite picture of the lava dome showing the points where the different lines of sight intersect the surface. The color coding corresponds to the density radiography and the thickness of rock traversed for each line of sight, respectively. When observing these figures, it should be noted that the relative density

variations correspond to an average value through the whole trajectory inside the volcano, and not to the point where the circle is represented. We can observe in Fig. 8 c) that the high-density anomaly thus corresponds to lines of sight that have traversed the dome flanks in a region directly south of the summit, usually referred to as the "bulge" in the literature (Boudon et al., 2008; Rosas-Carbajal et al., 2016; Heap et al., 2021). This region is thought to consist of relatively fresh and dense rocks. Focusing on the lines of sight close to the South Crater and the Tarissan acid pond, we can interpret from Figs. 8 b) and c) that Tarissan is located in a region of overall lower bulk density than the South-Crater (CS). Finally, if we compare the relative density distribution to the rock thickness distribution, it is interesting that the color spatial distributions are not the same, suggesting that the density anomalies observed do not correspond to changes in the amount of rock traversed by the muons.

Figure 9 shows the equivalent tomography and bird view representations for the BR detector. Although this is a 3-panel detector, the spatial resolution is increased with respect to SNJ because the scintillator bars are smaller. The largest density anomalies are observed for $\theta < 80°$ and $\phi \in [260, 290]$, that is, for lines of sight that cross the same "bulge" region as in the SNJ radiography (cf. Fig. 9 b)). We also retrieve on this East muography an overlaying low-density region above zenith 70°. The low-density anomaly also seems to rise up to the surface below the South-Crater region, around azimuth $290 \pm 4°$. On this muography, though, the shallow low-density anomaly appears broader and spans over the whole azimuth range above zenith 75°, reaching the lowest values of -70% above azimuth 310°, and zenith 65°. This low-density region close to the surface corresponds to a superficial part of the dome on the north-west flank, which crosses highly-altered and clay-rich material, revealed during the 2009 landslide (Rosas-Carbajal et al., 2016; Heap et al., 2021). The main pits and craters, whose positions are projected on the BR muography, are part of a wide network of cavities spanning from the north fault to the Tarissan crater and expanding on the East flank. These structural features are expected to have a significant impact on the bulk density estimates.

4 DISCUSSION

In this section, we discuss the results obtained regarding the performance of our particle tracking algorithm, the implications of the density radiographies provided, and possible improvements in future works.

Our RANSAC-based muon tracking algorithm was already shown to outperform the straightness check tests used previously by our team in terms of the number of events reconstructed and the precision on the inferred trajectory (Bajou et al., 2022). Here, we did a more exhaustive performance test using GEANT4 simulations to test our algorithm against perfectly known particle trajectories. Moreover, our numerical simulations consider the secondary particles produced as a result of the interaction with the lead panel located at the center of our detector (cf. Fig. 4). The processing of the GEANT4-generated data is encouraging in the sense that our algorithm successfully tagged true muon hits as inliers and significantly mitigated secondary hits.

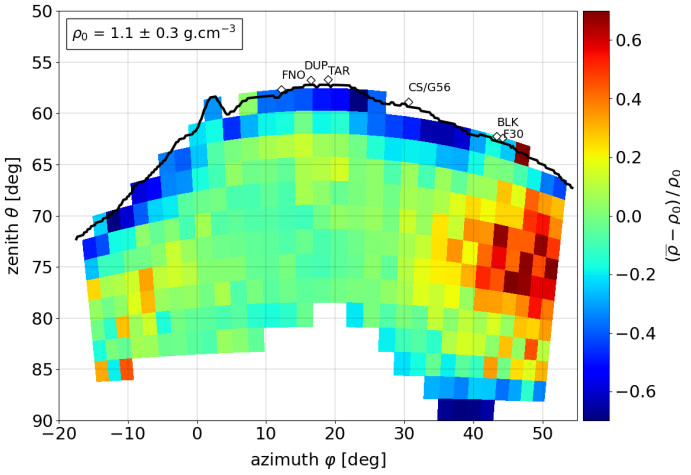

(a)

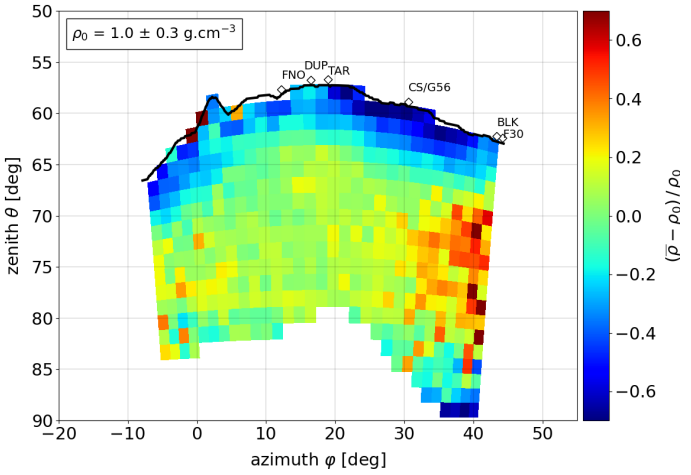

(b)

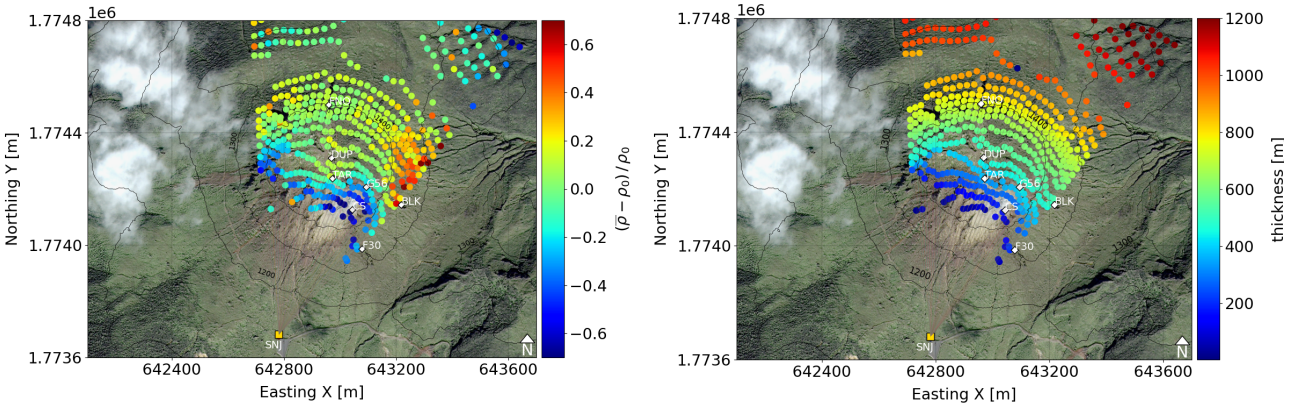

(c) (d)

Figure 8. Relative density variation two-dimensional maps estimated with the SNJ telescope (South-West) for (a) the three-panel configuration of SNJ (b) the four-panel configuration of SNJ. The map in (b) is projected onto the terrain model in (c): each line of sight (black line) features its density value, plotted at the entry point in the dome, and corresponds to a given dome thickness represented in (d). The main dome craters and pits positions of Fig. 1 are represented in blue lozenge markers.

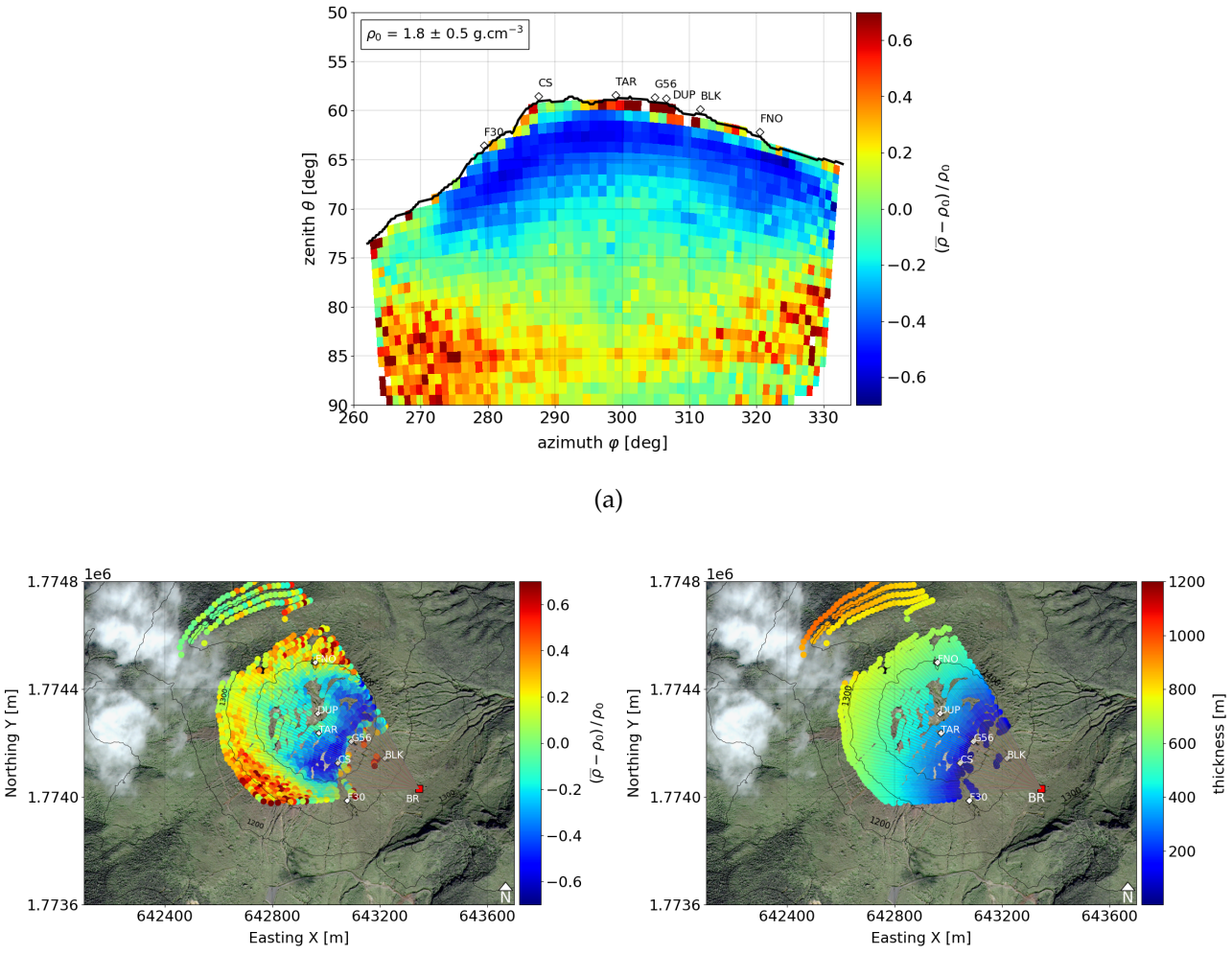

(a)

(b) (c)

Figure 9. Relative density variation map measured in BR telescope (East). The 2D density image in (a) is projected onto the terrain model in (b): each line of sight in black features its density value, plotted at the entry point in the dome, and corresponds to a given dome thickness on (c)

.

The comparison of real open-sky acquisitions with simulated data in equivalent conditions provides comparable results (cf. Fig. 6) and allows us to estimate the scintillator bars' efficiency. Our tracking algorithm is flexible in that it can be adapted to different geometries of scintillator panels. The main drawback is that it takes more time to run that the straightness check routines: $O(10^3\text{s})$ for 10^6 events on an 8-core CPU. Still, these are not prohibiting computation times considering that the analyses so far are not performed in real-time, and the significant improvement in data quality they provide.

The density spatial variations inferred from the real data acquisitions in La Soufrière de Guadeloupe can be qualitatively compared with a high-resolution electrical resistivity tomography of the

dome performed by Rosas-Carbajal et al. (2016), keeping in mind that rock conductivity is also influenced by other parameters such as rock porosity and fluid content. This work highlighted the presence of two distinct electrical conductivity regions: a low-conductivity shallow region named "bulge" on the south flank composed of non-altered dense andesitic rock, overlying a highly conductive region composed of mechanically weakened rock by hydrothermal activity. This bulge region scanned by both telescopes appears as the reddish high-density regions on the three muographies, for $\varphi > 30°$ in Fig. 8a and 8b, and $\varphi < 290°$ in Fig. 9a. On the other hand, the observed low-density region on the south flank is thought to correspond to the superficial part of the high-conductivity anomaly rising up to the dome summit.

As of today, this high electrical conductivity anomaly is understood to be the main pathway for hydrothermal acid fluids circulation, connecting southern thermal springs at the base of the lava dome to the dome summit. Surface manifestation of the arrival of these fluids includes continuous emission of sulfur and chlorine-rich gas through the fumarolic vents around Southern and Tarissan craters (cf. Fig.1a) (Moune et al., 2022). The continuous circulation of these fluids greatly contributes to the alteration and mechanical weakness of the dome rocks (Heap et al., 2021). Mechanical weakness is in part related to an increase in porosity, and thus it is reasonable that our muographies observe low-density values in highly altered regions as compared to fresh rock zones.

Among the structural features, several cavities of large volume inside the lava dome could have a significant impact on the observed densities. The BR muography featuring a broad low-density anomaly in Fig. 9 seems particularly impacted by the presence of such a network of cavities. In addition to the Tarissan and South craters, two additional pits of large size are located on the East-South-East flank: Breislack (BLK) and Gouffre 56 (G56), roughly 40 m deep (10% of the dome height), according to the description made by Kuster & Slive (1997), around azimuth $305°$ and $312°$. Another important cavity, the Spallanzani cave of volume 55x35x11m^3 (Kuster & Slive, 1997), whose entrance is located in the north fault (FNO), is also likely to have an impact on the mean density measurement. The effect on the density of such volume was already estimated between 10 to 15% by Lesparre et al. (2012b). As these cavities are currently not taken into account when computing the total dome thickness traversed by the muons, shown in Fig. 8d 9c, these void spaces add to an average bulk density significantly lower than the average value of actual rocks. The western superficial low-density anomaly that appears in Fig. 8a and b may also be caused by the existing network of cavities, expanding to the west. Nevertheless, the cavities delimitation is not well-documented in this area of the dome. As this low-density anomaly concerns the most superficial part of the dome and thus the shortest thicknesses L (cf. Fig. 8d) it is also likely to be affected by a systematic error on telescope orientation, whose impact on density estimation is important on this thinnest part of the dome. For the shallowest lines of sight of Fig. 8a and 8b covering a band of 3 pixels wide below the topographic profile (black line), we estimate that a 1-degree shift in both telescope azimuth and elevation gives

a mean relative error $\langle \Delta L/L \rangle = 0.21 \pm 0.12$, while for the rest of deeper lines of sights, this error reaches down to 0.09 ± 0.04. In the future, we intend to further develop the simulation tools to reproduce the geometry of the main cavities and provide a better characterization of their impact on the mean density estimates.

The telescopes are ideally located to scan what is thought to be the most-altered and collapse-prone part of the lava dome on the south flank. A downside of their closeness to the volcano flanks is that for lines of sight close to the horizon, that is, for large zenith values, there is a high probability of exposition to a particular source of noise contamination. This contamination comes from irreducible background sources such as the forward scattering effect of low-energy muons.

Previous studies (Nishiyama et al., 2016; Gómez et al., 2017; Chen et al., 2023) have indeed enlightened that for such large targets as volcanoes, flux measurements are strongly impacted by low-energy muons that are forward-scattered on the volcano flank facing the detector. These "soft" muons typically in the sub-GeV energy range can mimic dome-outgoing muon tracks and be reconstructed as such. This results in a measured flux that is over-estimated, which in turn leads to a lower opacity and thus lower average density estimate along the impacted line-of-sight. Indeed, this can be clearly observed in Fig. 8a and b for zenith angles higher than 85 degrees. Rock thicknesses in this area are so large that no muon events should be detected, therefore the low-density estimates arise from a large amount of forward scattered muons. Another source of contamination lies in the muon flux produced in the atmosphere below the telescope altitude. This backward muon flux can enter the telescope by its rear matrix, which especially impacts the most horizontal lines of sight above $\theta > 80°$ and can significantly blur muon radiography close to the horizon, accounting for up to 50% of the detected events (Jourde et al., 2014). The ideal rejection for this upward flux requires an ns clocking system for a precise time-of-flight measurement.

Gómez et al. (2017) have shown for a simplified cone-shaped dome geometry that the forward scattering of muons increases with the zenith angle θ, exceeding 50% of the total number of reconstructed events for θ superior to 85°. This background noise is also location-dependent and thus requires specific estimation for each muon imaging study. To cope with this irreducible background noise and infer realistic absolute density values, the simulation setup presented in Sec. 2.4 is expected to provide the right framework to accurately estimate the percentages of forward-scattered to outgoing muons. We leave these developments for a future contribution.

5 CONCLUSION

We presented a new muon tracking algorithm to process data from 3- and 4-panel scintillator-based muon detectors. Our algorithm successfully captures muon hits and rejects outlier hits formed by secondary particles in the telescope data. We have also developed simulation tools that show that

our new algorithm outperforms previously used ones based on straight-line analyses. Furthermore, we can use these simulations to reconstruct our scintillator's efficiency and study the experimentally calibrated acceptance against the simulation predictions.

Our algorithm was successfully applied to estimate muon density radiographies of La Soufrière with data acquired by a new generation of muon telescopes. The density variations have an improved spatial resolution with respect to previous works and are overall in agreement with previous studies. Although the absolute mean density estimates are biased by irreducible background sources, the relative mean density radiographies still reflect the heterogeneous structure of the dome, thanks to long and steady runs of data acquisition obtained in the two different detectors.

Future work will focus on correcting the two-dimensional muographies from systematic effects such as muon forward scattering, and in the following, on performing data inversion on the corrected density maps to obtain a realistic three-dimensional density model of the dome. The forward scattering correction will be a natural improvement using the GEANT4 simulations developed in this study. The topography of the terrain surrounding each detector has key importance in this matter. It can now be reproduced with the implementation of the digital terrain model in the presented GEANT4 framework. As an alternative to GEANT4, we also mention the PUMAS library (Niess, 2022) that could also be used for scattering correction studies. This code is based on backward Monte-Carlo to perform muon transport in matter and was initially developed for muography applications. Furthermore, implementing the geometry of the main known geological structural features of the lava dome, fractures, faults, and craters is also possible and will greatly improve the quality of our radiographies and therefore of the three-dimensional density models obtained with them.

ACKNOWLEDGMENTS

This work and the data shown were acquired in the context of two projects supported by the French Agence Nationale de la Recherche, projects DIAPHANE (ANR-14-ce04-0001) and MEGaMu (ANR-19-CE05-0033). We thank the editor C. Sens-Schönfelder, reviewer R. Nishiyama, and an anonymous reviewer, whose comments have contributed to improving the quality of our manuscript. The simulation and data analysis were performed on the S-CAPAD/DANTE platform of IPGP, France.

DATA AVAILABILITY

The data presented in this work are not publicly available.

References

Agostinelli, S., Allison, J., Amako, K., Apostolakis, J., & et al., 2003. Geant4—a simulation toolkit, *Nuclear Instruments and Methods in Physics Research Section A: Accelerators, Spectrometers, Detectors and Associated Equipment*, **506**(3), 250–303.

Alvarez, L., Anderson, J., Bedwei, F., Burkhard, J., Fakhry, A., Girgis, A., Goneid, A., Hassan, F., Iverson, D., Lynch, G., Miligy, Z., Moussa, A., Sharkawi, M., & Yazolino, L., 1970. Search for hidden chambers in the pyramids, *Science (New York, N.Y.)*, **167**, 832–9.

Bajou, R., Rosas-Carbajal, M., & Marteau, J., 2022. A New Versatile Method for the Reconstruction of Scintillator-Based Muon Telescope Events, *JAIS*, **2022**(1), 254.

Ball, J., Stauffer, P., Calder, E., & Valentine, G., 2015. The hydrothermal alteration of cooling lava domes, *Bulletin of Volcanology*, **77**.

Barnoud, A., Cayol, V., Lelièvre, P. G., Portal, A., Labazuy, P., Boivin, P., & Gailler, L., 2021. Robust Bayesian Joint Inversion of Gravimetric and Muographic Data for the Density Imaging of the Puy de Dôme Volcano (France), *Frontiers in Earth Science*, **8**, co-auteur étranger.

Bonechi, L., D'Alessandro, R., & Giammanco, A., 2020. Atmospheric muons as an imaging tool, *Reviews in Physics*, **5**, 100038.

Boudon, G., Komorowski, J.-C., Villemant, B., & Semet, M. P., 2008. A new scenario for the last magmatic eruption of la soufrière of guadeloupe (lesser antilles) in 1530 a.d. evidence from stratigraphy radiocarbon dating and magmatic evolution of erupted products, *Journal of Volcanology and Geothermal Research*, **178**(3), 474–490, Evaluating Explosive Eruption Risk at European Volcanoes.

Chen, L., Zhang, L., Cheng, Y., Laktineh, I., & Han, R., 2023. Monte Carlo simulation for background noise study of the Wudalianchi volcanic density imaging, *Nuclear Instruments and Methods in Physics Research Section A: Accelerators, Spectrometers, Detectors and Associated Equipment*, **1048**, 167971.

Cohu, A., Tramontini, M., Chevalier, A., Ianigro, J.-C., & Marteau, J., 2022. Atmospheric and Geodesic Controls of Muon Rates: A Numerical Study for Muography Applications, in *19th International Conference on Calorimetry in Particle Physics*, vol. 6, p. 24, Brighton, United Kingdom.

D'Alessandro, R., Ambrosino, F., Baccani, G., Bonechi, L., Bongi, M., Caputo, A., Ciaranfi, R., Cimmino, L., Ciulli, V., d'Errico, M., Giudicepietro, F., Gonzi, S., Macedonio, G., Masone, V., Melon, B., Mori, N., Noli, P., Orazi, M., del Vecchio Passeggio, P., Peluso, R., Saracino, G., Scognamiglio, L., Strolin, P. E., Vertechi, E., & Viliani, L., 2018. Volcanoes in italy and the role of muon radiography, *Philosophical Transactions of the Royal Society A*, **377**.

Fischler, M. A. & Bolles, R. C., 1981. Random sample consensus: a paradigm for model fitting with applications to image analysis and automated cartography, *Communications of the ACM*.

Gaisser, T. K., Engel, R., & Resconi, E., 1990. *Cosmic Rays and Particle Physics*, Cambridge University Press, 2nd edn.

Gómez, H., Goy, C., Karyotakis, Y., Katsanevas, S., Marteau, J., Tonazzo, A., Gibert, D., Jourde, K., & Rosas-Carbajal, M., 2017. Forward scattering effects on muon imaging, *JINST*, **12**(12), P12018.

Gonidec, Y. L., Rosas-Carbajal, M., d'Ars, J. d. B., Carlus, B., Ianigro, J.-C., Kergosien, B., Marteau, J., & Gibert, D., 2019. Abrupt changes of hydrothermal activity in a lava dome detected by combined seismic and muon monitoring.

Guan, M., Chu, M.-C., Cao, J., Luk, K.-B., & Yang, C., 2015. A parametrization of the cosmic-ray muon flux at sea-level, *arXiv e-prints*, p. arXiv:1509.06176.

Heap, M. & Violay, M. E., 2021. The mechanical behaviour and failure modes of volcanic rocks: a review, *Bulletin of Volcanology*, **83**(5), 33, Publisher: Springer Verlag.

Heap, M. J., Baumann, T. S., Rosas-Carbajal, M., Komorowski, J.-C., Gilg, H. A., Villeneuve, M., Moretti, R., Baud, P., Carbillet, L., Harnett, C., & Reuschlé, T., 2021. Alteration-induced volcano instability at la soufrière de guadeloupe (eastern caribbean), *Journal of Geophysical Research: Solid Earth*, **126**(8), e2021JB022514, e2021JB022514 2021JB022514.

Heck, D., Knapp, J., Capdevielle, J.-N., Schatz, G., & Thouw, T., 1998. CORSIKA: A Monte Carlo Code to Simulate Extensive Air Showers, pp. 1–90.

Jourde, K., Gibert, D., Marteau, J., de Bremond d'Ars, J., Gardien, S., Girerd, C., Ianigro, J.-C., & Carbone, D., 2014. Experimental detection of upward-going cosmic particles and consequences for correction of density radiography of volcanoes, in *European Geosciences Union General Assembly 2014*, vol. 16, pp. EGU2014–9985, Vienne, Austria.

Jourde, K., Gibert, D., Marteau, J., de Bremond d'Ars, J., & Komorowski, J.-C., 2016. Muon dynamic radiography of density changes induced by hydrothermal activity at the La Soufrière of Guadeloupe volcano, *Scientific Reports*, **6**(1), 33406.

Komorowski, J.-C., B. G. S. M. B. F. A.-H. C. B. S. . H. G., 2005. Guadeloupe, in *Volcanic Atlas of the Lesser Antilles*, pp. 65–102, University of the French West Indies, Seismic Research Unit.

Kuster, D. & Slive, V., 1997. *Guadeloupe, Canyons, Gouffres, Découverte*.

Lechmann, A., Mair, D., Ariga, A., Ariga, T., Ereditato, A., Nishiyama, R., Pistillo, C., Scampoli, P., Schlunegger, F., & Vladymyrov, M., 2021. Muon tomography in geoscientific research – a guide to best practice, *Earth-Science Reviews*, **222**, 103842.

Lesparre, N., Marteau, J., Déclais, Y., Gibert, D., Carlus, B., Nicollin, F., & Kergosien, B., 2012a. Design and operation of a field telescope for cosmic ray geophysical tomography, *Geoscientific Instrumentation, Methods and Data Systems*, **1**, 33–42.

Lesparre, N., Gibert, D., Marteau, J., Komorowski, J.-C., Nicollin, F., & Coutant, O., 2012b. Density muon radiography of La Soufrière of Guadeloupe volcano: comparison with geological, electrical resistivity and gravity data, *Geophysical Journal International*, **190**(2), 1008–1019.

Lo Presti, D., Riggi, F., Ferlito, C., Bonanno, D. L., Bonanno, G., Gallo, G., La Rocca, P., Reito, S., & Romeo, G., 2020. Muographic monitoring of the volcano-tectonic evolution of Mount Etna,

Scientific reports, **10**(1), 11351.

Marteau, J., 2009. The OPERA global readout and GPS distribution system, in *11th Pisa Meeting on Advanced Detectors*, vol. 617, pp. 291–293, La Biodola, Italy.

Marteau, J., Gibert, D., Lesparre, N., Nicollin, F., Noli, P., & Giacoppo, F., 2012. Muons tomography applied to geosciences and volcanology, *Nuclear Instruments and Methods in Physics Research Section A: Accelerators, Spectrometers, Detectors and Associated Equipment*, **695**, 23–28.

Marteau, J., Carlus, B., Gibert, D., Ianigro, J.-C., Jourde, K., Kergosien, B., & Rolland, P., 2016. Muon tomography applied to activevolcanoes, p. 004.

Moretti, R., Komorowski, J.-C., Ucciani, G., Moune, S., Jessop, D., Chabalier, J.-B. d., Beauducel, F., Bonifacie, M., Burtin, A., Vallee, M., Deroussi, S., Robert, V., Gibert, D., Didier, T., Kitou, T., Feuillet, N., Allard, P., Tamburello, G., Shreve, T., Saurel, J.-M., Lemarchand, A., Rosas-Carbajal, M., Agrinier, P., Le Friant, A., & Chaussidon, M., 2020. The 2018 unrest phase at la soufrière of guadeloupe (french west indies) andesitic volcano: Scrutiny of a failed but prodromal phreatic eruption, **393**, 106769.

Moune, S., Moretti, R., Burtin, A., Jessop, D. E., Didier, T., Robert, V., Bonifacie, M., Tamburello, G., Komorowski, J.-C., Allard, P., & Buscetti, M., 2022. Gas Monitoring of Volcanic-Hydrothermal Plumes in a Tropical Environment: The Case of La Soufrière de Guadeloupe Unrest Volcano (Lesser Antilles), *Frontiers in Earth Science*, **10**.

Nagamine, K., Iwasaki, M., Shimomura, K., & Ishida, K., 1995. Method of probing inner-structure of geophysical substance with the horizontal cosmic-ray muons and possible application to volcanic eruption prediction, *Nuclear Instruments and Methods in Physics Research Section A: Accelerators, Spectrometers, Detectors and Associated Equipment*, **356**(2), 585–595.

Niess, V., 2022. The PUMAS library, *Computer Physics Communications*, **279**, 108438.

Nishiyama, R., Taketa, A., Miyamoto, S., & Kasahara, K., 2016. Monte carlo simulation for background study of geophysical inspection with cosmic-ray muons, **206**(2), 1039–1050.

Nishiyama, R., Miyamoto, S., Okubo, S., Oshima, H., & Maekawa, T., 2017. 3d density modeling with gravity and muon-radiographic observations in showa-shinzan lava dome, usu, japan, *Pure and Applied Geophysics*, **174**.

Peruzzetto, M., Komorowski, J.-C., Le Friant, A., Rosas-Carbajal, M., Mangeney, A., & Legendre, Y., 2019. Modeling of partial dome collapse of la soufrière of guadeloupe volcano: implications for hazard assessment and monitoring, *Scientific Reports*, **9**.

Peña-Rodríguez, J., Pisco-Guabave, J., Sierra-Porta, D., Suárez-Durán, M., Arenas-Flórez, M., Pérez-Archila, L. M., Sanabria-Gómez, J. D., Asorey, H., & Núñez, L. A., 2020. Design and construction of mute: a hybrid muon telescope to study colombian volcanoes.

Rosas-Carbajal, M., Komorowski, J.-C., Nicollin, F., & Gibert, D., 2016. Volcano electrical tomography unveils edifice collapse hazard linked to hydrothermal system structure and dynamics, *Scien-*

tific Reports, **6**(1), 29899.

Rosas-Carbajal, M., Jourde, K., Marteau, J., Deroussi, S., Komorowski, J.-C., & Gibert, D., 2017. Three-dimensional density structure of La Soufrière de Guadeloupe lava dome from simultaneous muon radiographies and gravity data, *Geophysical Research Letters*, **44**(13), 6743–6751.

Saracino, G., Ambrosino, F., Bonechi, L., Bross, A., Cimmino, L., Ciaranfi, R., D'Alessandro, R., Giudicepietro, F., Macedonio, G., Martini, M., Masone, V., Mori, N., Noli, P., Orazi, M., Passeggio, G., Pla-Dalmau, A., Roscilli, L., & Strolin, P., 2016. The muraves muon telescope: technology and expected performances, *Annals of Geophysics*, **60**(1).

Siebert, L., Simkin, T., & Kimberly, P., 2011. *Volcanoes of the World*, vol. 349.

Sullivan, J., 1971. Geometric factor and directional response of single and multi-element particle telescopes, *Nuclear Instruments and Methods*, **95**(1), 5–11.

Tamburello, G., Moune, S., Allard, P., Venugopal, S., Robert, V., Rosas-Carbajal, M., Deroussi, S., Kitou, G.-T., Didier, T., Komorowski, J., Beauducel, F., de Chabalier, J. B., Marchand, A. L., Friant, A. L., Bonifacie, M., Dessert, C., & Moretti, R., 2019. Spatio-temporal relationships between fumarolic activity, hydrothermal fluid circulation and geophysical signals at an arc volcano in degassing unrest: La soufrière of guadeloupe (french west indies), *Geosciences*.

Tanaka, H., Nagamine, K., Kawamura, N., Nakamura, S. N., Ishida, K., & Shimomura, K., 2003. Development of a two-fold segmented detection system for near horizontally cosmic-ray muons to probe the internal structure of a volcano, *Nuclear Instruments and Methods in Physics Research, Section A: Accelerators, Spectrometers, Detectors and Associated Equipment*, **507**(3), 657–669.

Tanaka, H. K. M., 2018. Japanese volcanoes visualized with muography, *Philosophical Transactions of the Royal Society A*, **377**.

Thomas, G. R. & Willis, D. M., 1972. Analytical derivation of the geometric factor of a particle detector having circular or rectangular geometry, *Journal of Physics E: Scientific Instruments*, **5**(3), 260.

van der Walt, S., Schönberger, J. L., Nunez-Iglesias, J., Boulogne, F., Warner, J. D., Yager, N., Gouillart, E., Yu, T., & the scikit-image contributors, 2014. scikit-image: image processing in Python, *PeerJ*, **2**, e453.

Workman, R. L. & Others, 2022. Review of Particle Physics, *PTEP*, **2022**, 083C01.